Editors' Suggestion

Impact of turbulence on flying insects in tethered and free flight: High-resolution numerical experiments

Thomas Engels*
LMD-IPSL, École Normale Supérieure-PSL, 24 Rue Lhomond, 75231 Paris Cedex 05, France

Dmitry Kolomenskiy
Japan Agency for Marine-Earth Science and Technology (JAMSTEC), 3173-25 Showa-machi, Kanazawa-ku, Yokohama Kanagawa 236-0001, Japan

Kai Schneider
Aix-Marseille Université, CNRS, Centrale Marseille, I2M UMR 7373, Marseille, 39 rue Joliot-Curie, 13451 Marseille Cedex 20, France

Marie Farge
CNRS-INSMI, LMD-IPSL, École Normale Supérieure-PSL, 24 Rue Lhomond, 75231 Paris Cedex 05, France

Fritz-Olaf Lehmann
Department of Animal Physiology, Universität Rostock, Rostock, Albert-Einstein-Strasse 3, 18059 Rostock, Germany

Jörn Sesterhenn
ISTA, Technische Universität Berlin, Müller-Breslau-Strasse 12, 10623 Berlin, Germany

(Received 22 April 2018; published 16 January 2019)

Flapping insects are remarkably agile fliers, adapted to a highly turbulent environment. We present a series of high-resolution numerical simulations of a bumblebee interacting with turbulent inflow. We consider both tethered and free flight, the latter with all six degrees of freedom coupled to the Navier-Stokes equations. To this end, we vary the characteristics of the turbulent inflow, either changing the turbulence intensity or the spectral distribution of turbulent kinetic energy. Active control is excluded in order to quantify the passive response real animals exhibit during their reaction time delay, before the wing beat can be adapted. Modifying the turbulence intensity shows no significant impact on the cycle-averaged aerodynamical forces, moments, and power, compared to laminar inflow conditions. The fluctuations of aerodynamic observables, however, significantly grow with increasing turbulence intensity. Changing the integral scale of turbulent perturbations, while keeping the turbulence intensity fixed, shows that the fluctuation level of forces and moments is significantly reduced if the integral scale is smaller than the wing length. Our study shows that the scale-dependent energy distribution in the surrounding turbulent flow is a relevant factor conditioning how flying insects control their body orientation.

DOI: 10.1103/PhysRevFluids.4.013103

*thomas.engels@ens.fr

I. INTRODUCTION

Insect are fast and agile fliers and stabilize their body posture during flight under a vast variety of environmental conditions [1,2]. While flight in static air requires little steering and corrective changes in aerodynamic force production, flight in turbulent air is challenged by unexpected changes in flow conditions at the body and wings. Little is known about the impact of turbulence on the aerodynamic performance and energetic cost of flight in insects. In this work, we study how different kinds of perturbations affect flapping fliers in free flight.

In contrast to laminar flows, turbulent flows are dominated by nonlinear interactions and, as a result, excite fluctuations on a wide range of scales. After averaging the flow in either ensemble, time, or space, we identify different length scales characteristic for the turbulent regime. From large to small, these classical scales are (i) the integral scale Λ where, on average, the velocity the strongest and where therefore energy transport is most active, (ii) the Taylor microscale λ where, on average, the velocity gradients are most intense, and (iii) the Kolomogorov scale η below which, on average, the flow fluctuations are damped by the fluid viscosity [3].

In nature, unsteady turbulent flow conditions significantly vary depending on the terrain and weather conditions. The "flight boundary layer," characterized by conditions favorable for insect flight, can span up to 1500 m above the ground level in warm weather [4]. Activity such as long-distance migration is typical of high altitudes while foraging, for example, mainly takes place in the vegetation layer up to several meters above the ground. This diversity of flow conditions, besides variation in the temperature, density, and mean wind speed, exposes flying insects to a variety of turbulent flows, ranging from those dominated by wakes and canopy-layer turbulence at low altitude [5–7] to the atmospheric turbulence determined by weather and wind systems at high altitude [8,9].

Until now, studies have focused on selected model organisms such as hummingbirds [10], moths [11,12], and bumblebees [13,14], subject to archetypal air flow conditions such as von Kármán wakes [12–14] or grid turbulence [15]. In the hawk moths *Manduca sexta*, for example, yaw and roll oscillations of the animal body are synchronized with the vortex shedding frequencies in the wake behind a large cylinder [12]. Vortex shedding in von Kármán wakes, however, differs from turbulence since, at moderate Reynolds numbers, vortices are shed periodically in time and the flow has strong spatial correlations. Few numerical [16] and experimental [15,17] studies addressed flapping flight in turbulent flow and estimated flow conditions at body and wings. In heavy turbulence, for example, bumblebees are highly prone to changes in roll stability and crash if roll velocity exceeds a maximum value [15].

High maneuverability in flight is likely key in coping with turbulence, at the cost of low stability [11,18]. Insects that stabilize their body posture during aerial perturbations thus require fast feedback responses. These responses may rely on passive and active changes of wing and body kinematics. Both mechanisms might help to mitigate aerial perturbations. While passive changes of wing kinematics result from the interplay between wing material properties and inertial and aerodynamic forces and thus elastic wing deformation [19–24], active control is imposed by the sensomotor system of the animal and thus changes in flight muscle activation [25]. A complex passive mechanism has been reported for the fruit fly *Drosophila* [26]. The latter study suggests that wing rotation about the wing' s longitudinal axis [21] behaves like a system composed of a damped torsion spring. The animal might control wing rotation by actively changing stiffness and damping coefficients of this spring, as well as the resting feathering angle. In this case, fluid-structure interaction results from a combination of passive changes via spring deformation and active changes via modifications of the spring' s elastic property.

Besides passive changes, insects also possess a large variety of active control mechanisms for body stabilization and flight heading control. Studies on flight control highlighted several unique mechanisms of wing motion modulation in insects (see Ref. [27] for a recent review). These mechanisms include changes in stroke amplitude, stroke frequency, stroke plane, the wing's angle of attack, and timing of wing rotation at the end of each half stroke [15,28]. Freely flying bumblebees, for example, stabilize body roll by changes of the relative difference between left and right stroke

amplitude [17]. Insects also actively change body shape that modifies their inertia tensor during flight. Fruit flies [29], hawk moths [30], and chestnut tiger butterflies [31], for example, change and stabilize their flight heading by changing the angle between thorax and abdomen.

Previous studies considered the body roll axis of an animal to be most susceptible for aerodynamic perturbations, owing to its small moment of inertia compared to yaw and pitch. Flying through turbulence thus produces largest fluctuations about the roll axis in insects [13]. To minimize these changes, some insects laterally extend their hind legs, which increases the roll moment of inertia [15]. Although this behavior has been found in orchid bees, smaller insects such as the fruit fly benefit only little from this mechanism owing to their small legs [29]. Since the hind legs of orchid bees are atypically large compared to other insect species, it is less likely that the latter mechanism represents a common mechanism for roll control in insect flight [29]. A most significant mechanism to cope with air turbulence is aerodynamic damping, resulting from the flapping wing motion. It is termed flapping countertorque [11,18,32] and primarily acts in the direction perpendicular to the stroke plane. In a horizontal stroke plane, roll damping only occurs if left and right wings flap at different angle of attack [33]. In an inclined stroke plane, the moment vector is deflected from the vertical and contributes to roll dynamics, even during symmetrical motion of both wings. The concept of flapping countertorque in insects was extended to damping coefficients for all six degrees of freedom of body motion [34].

To understand body posture control of insects flying in turbulent air, we here present a numerical study. Our study models and compares flight of both tethered and freely flying insects (bumblebees). We consider different turbulent flows and vary their turbulence intensity as well as their characteristic length scales, e.g., the integral scale. Under free flight conditions, the model insect is allowed to translate along and rotate about all three body axes, in response to aerodynamic, inertial, and gravitational forces and moments. However, we exclude any active control in this work.

Our previous study [16] showed that in tethered flight even strong inflow turbulence has little effect on mean force production and moments and thus on aerodynamic mechanisms. Building on this finding, we here explore the effects of turbulent length scales on a freely flying insect model and demonstrate the effect of turbulence on body posture in free flight. The approach allows body motion but ignores any *passive* deformation, of both body and wing, and also *active* steering. Our study investigates if and how the scale-dependent energy distribution is relevant for body orientation control in flying insects.

The complicated time-dependent geometry and the resulting complex flow topology challenge numerical simulations of insect flight. There are two major numerical approaches for this problem: (i) overset grids [35–37], which allow strong refinement near surfaces, but consideration of inflow turbulence is practically excluded because of difficulties in parallelization and hence limited resolution, and (ii) immersed boundary methods (IBM), which disconnect the flapping motion from the grid and thus simplify the discretization. For flapping flight, finite volume [38,39] or lattice-Boltzmann-type simulations [40,41] are successful numerical methods combined with IBM. Here, we use the volume penalization method combined with a Fourier pseudospectral solver [42]. This numerical method is characterized by the absence of numerical dissipation, its high efficiency on massively parallel computers due to the optimized implementation of FFTs [43], and the possibility to impose turbulent inflow.

The remainder of the paper is organized as follows: The computational setup is illustrated in Sec. II A and the characteristics of inflow turbulence are described in Sec. II B. Section II C presents the bumblebee model and Sec. II D recalls the governing equations and briefly outlines the numerical method. The results and discussion in Sec. III present first tethered flight simulations and then different free flight cases. Finally, conclusions are drawn in Sec. IV and some possible directions for future work are proposed.

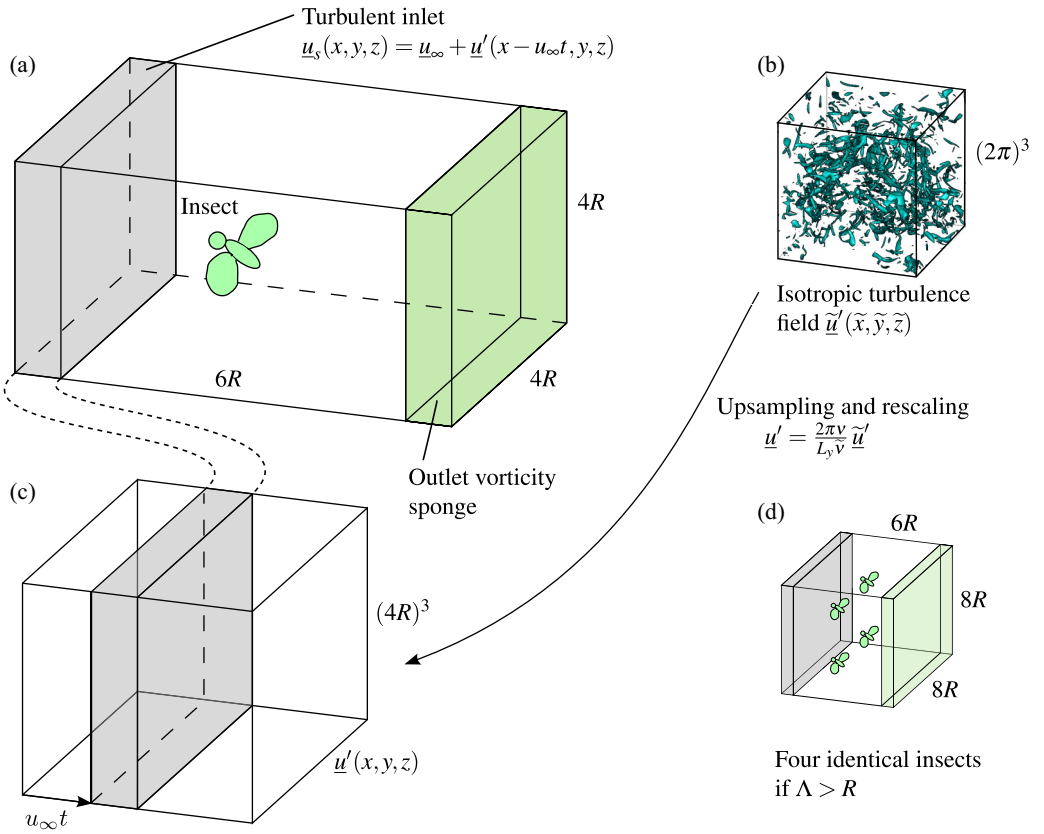

FIG. 1. Setup used in present work. (a) Numerical wind tunnel, with tethered or freely flying insects. Turbulent inflow is imposed in the upstream gray area; a vorticity sponge in the downstream green area damps vortices and thus minimizes their upstream influence. The turbulent inlet imposes a slice of an isotropic turbulence field (b), which has been precomputed in a separate simulation. The turbulence field has been upsampled (c) to match the resolution of the numerical wind tunnel and rescaled preserving dynamic similarity. The gray slice in panel (c) moves through the periodic field $\underline{u}'(x, y, z)$ at constant speed u_∞. In some simulations with larger integral scale Λ, four identical insects are computed (d) in one simulation, as explained in Sec. II B.

II. FLOW CONFIGURATION AND NUMERICAL METHOD

A. Numerical wind tunnel

We illustrate the computational setup and the flow configuration in Fig. 1. Simulations are performed in a $6R\times4R\times4R$ large virtual wind tunnel [Fig. 1(a)], where R is the wing length of the insect (see Sec. II C). We initially place the insect at $\underline{x}_{\text{cntr}} = (2R,\ 2R,\ 2R)^T$ and either allow it to move freely as dictated by the fluid forces or tether it to that position. The resolution in space is $1152\times768\times768$ equidistant grid points, and thus the lattice spacing is $\Delta = 5.2\times10^{-3}R$. The mean flow velocity is set to $\underline{u}_\infty = (1.246\,Rf,\ 0,\ 0)^T$, where f is the wing beat frequency. It compensates for the cruising speed of the insect in laminar flow. We initialize the simulation with unperturbed, laminar flow, $\underline{u}(\underline{x}, t = 0) = \underline{u}_\infty$. At the outlet, a vorticity sponge [44] minimizes the upstream influence of the periodicity of the computational domain. In the inlet region, which covers the first 48 grid points, the velocity is set to $\underline{u}_s = \underline{u}_\infty + \underline{u}'$, where $\underline{u}'$ are velocity fluctuations obtained from a precomputed, homogeneous isotropic turbulence (HIT) velocity field [Fig. 1(b)]. The properties of this field are discussed in Sec. II B.

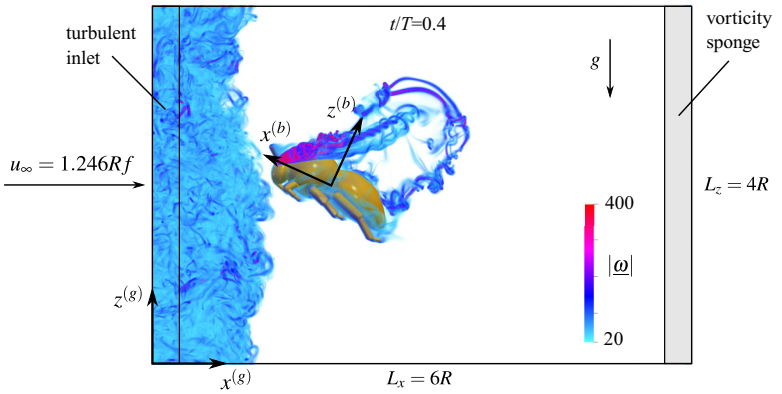

FIG. 2. Snapshot of a simulation. The virtual bumblebee is tethered in the virtual wind tunnel; the mean flow u_∞ in the $x^{(g)}$ direction compensates for the cruising speed of the insect. Reference frames shown are the global (g) and body fixed (b). The flow field is visualized by the vorticity magnitude at an early instant ($t = 0.4T$) before the laminar-turbulent interface reaches the insect. The parameters are $I = 0.99$ and $\Lambda = 0.77R$.

We rescale the HIT velocity field to insect dimensions preserving dynamic similarity, as HIT simulations are typically performed in a dimensionless manner. The field is then upsampled using zero padding in Fourier space to match the resolution of the numerical wind tunnel [Fig. 1(c)]. Note that the resolution requirement for the bumblebee is larger than for the HIT simulations in all considered cases, as required by the detailed geometry of the bumblebee. In cases with larger integral scale, we compute four identical bumblebees in one simulation with doubled lateral domain size and the same resolution [Fig. 1(d)], for reasons explained below.

Figure 2 shows an example computation. Inside the inlet layer, the HIT field is frozen, i.e., not dynamically evolving. Further downstream the turbulent flow evolves dynamically, and decays similarly to what is observed in grid turbulence. The imposed constant mean flow u_∞ transports the turbulent-laminar interface, as illustrated in Fig. 2. It reaches the insect's head at $t/T = 0.95$ and its tail at $t/T = 1.95$. Thus, all wing beats after the second one take place in turbulence and are used to compute the statistics. After $t/T = 3.21$, the periodic HIT field repeats, owing to the spatial periodicity of the precomputed field. For each statistical state of inflow turbulence, we compute a number of realizations N_R to be able to perform ensemble averaging. All simulations are identical except for the turbulent inflow field. For more technical details, we refer to Ref. [16, Suppl. Mat.].

B. Inflow turbulence

Flying animals encounter a considerable variety of aerial perturbations while foraging, ranging from no perturbation in almost quiescent air when the weather is calm, to fully turbulent, with intermittent gusts and vortices generated by obstacles, such as flowers, trees, or buildings. The type of perturbation also depends on behavioral patterns in animals. Bees, for example, forage on flowers and thus regularly perform landing maneuvers which force them to fly in the flower's wake. Owing to this huge variability in turbulent perturbations, we first reduce the parameter space. Therefore, we define a typical turbulent flow and choose homogeneous isotropic turbulence (HIT) for the upstream perturbations because it is the most widely used. It is also realized in experimental work, e.g., generated by a grid in a wind tunnel [17]. HIT is characterized by its turbulent kinetic energy $E = 3u_{\mathrm{RMS}}^2/2$, or equivalently the turbulence intensity $I = u_{\mathrm{RMS}}/u_\infty$, the Reynolds number

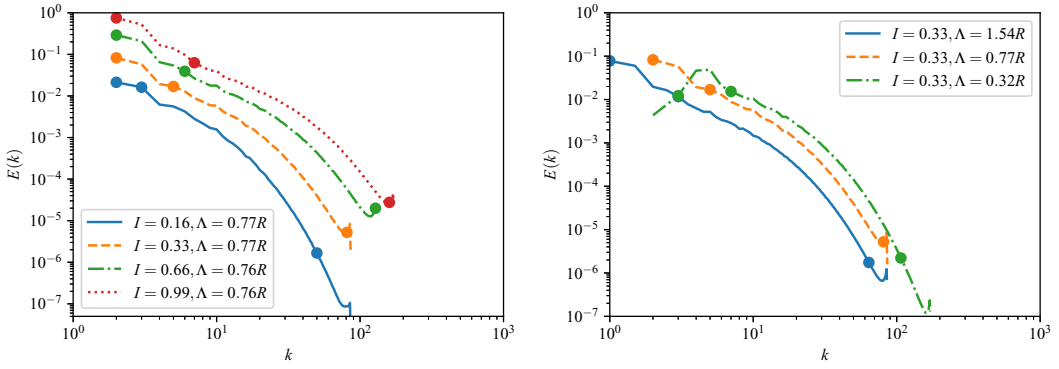

FIG. 3. Spectra of turbulent kinetic energy for HIT fields averaged over several eddy turnover times. Left: series A with constant Λ and variable I; right: series B for $I = 0.33$ and Λ variable. Markers are the wave numbers associated with Λ, λ, and η (from left to right on each spectrum).

$\mathrm{Re}_\lambda = u_{\mathrm{RMS}}\lambda/\nu$, based on the Taylor microscale $\lambda = \sqrt{15\nu u_{\mathrm{RMS}}/\varepsilon}$, and the integral length scale

$$\Lambda = \frac{\pi}{2u_{\mathrm{RMS}}^2}\int_{k>0}^{\infty} k^{-1}E(k)\,dk\,.$$

Here, ν is the kinematic viscosity, ε is the dissipation rate, k is the wave number, and $E(k)$ is the energy spectrum integrated over wave-number shells. Note that for spatially periodic velocity fields, the integral reduces to a sum, as only integer wave numbers $k \in \mathbb{N}$ exist. We precompute the HIT velocity fields in a separate direct numerical simulation. In this computation, energy is injected at a given wave number k_f to compensate for the loss due to viscous dissipation. Forced wave numbers in the shell $k_f - 0.5 \leqslant |k| \leqslant k_f + 2.5$ are multiplied with a factor $c(t)$ to keep the overall energy constant in time. This approach is known as negative viscosity forcing [45,46]. In all HIT computations, we resolve the Kolmogorov scale $\eta = (\nu^3/\varepsilon)^{1/4}$, and hence $k_{\max}\eta \gtrsim 1$. We start the HIT simulations with a random initial condition with prescribed spectrum [47]. After the statistically steady state has been reached, we save velocity fields for later use as inflow perturbations. The saving interval is at least 10 eddy turnover times to assure that the fields are uncorrelated in time. By modifying k_f at constant E and ν, we vary the spectral distribution of energy.

We generate two series of HIT simulations with turbulent kinetic energy spectra shown in Fig. 3. In series A, we vary the intensity I from mildly ($I = 0.16$) to extremely ($I = 0.99$) turbulent while keeping the integral length scale $\Lambda = 0.77R$ fixed (Fig. 3 left). In series B, we fix $I = 0.33$ and vary $\Lambda = \{0.32R,\ 0.77R,\ 1.54R\}$ (Fig. 3 right). Turbulence properties are summarized in Table I. The first series allows us to evaluate the impact of turbulence intensity, while the second series allows us to investigate the influence of Λ on the insect. Note that the eddy turnover time $T_0 = \Lambda/u_{\mathrm{RMS}}$ decreases, as expected, with increasing I (series A) and, likewise, with decreasing Λ (series B). We vary the energy distribution via the forcing wave number k_f in the HIT simulation. Note that in the $\Lambda = 0.77R$ case the forcing wave number was $k_f = 1$; thus, we cannot reduce it any further in order to increase Λ. Therefore, in order to increase Λ to $1.54R$, we double the lateral domain size to $L_y = L_z = 8R$ in the insect simulation, which then allows $k_f = 1$ to result in a larger integral scale. With the larger domain, we then compute four identical insects in one simulation [Fig. 1(d)], to reduce the computational cost.

Figure 4 illustrates two individual HIT fields from the B series by showing the isosurface of vorticity $|\underline{\omega}| = 4\sigma(\underline{\omega})$, where σ is the corresponding standard deviation. The energy E of both fields is the same, but the integral scales are $\Lambda = 1.54R$ and $0.32R$, respectively. Visibly, the $\Lambda = 0.32R$ case features smaller scale vortices which are more densely distributed in the periodic box.

TABLE I. Properties of the homogeneous isotropic turbulence fields (time averaged over several eddy-turnover times) used as inflow perturbations for the insect. The rightmost column shows the number of realizations N_R used in tethered and free flight simulations. Here, I is the turbulence intensity, which is equivalent to the turbulent kinetic energy, Λ is the integral scale, λ is the Taylor microscale, η is the Kolmogorov scale, and T_0 is the eddy turnover time. All quantities are given in units of wing length R and wing beat duration T.

								N_R	
Series	I	$\Lambda\,[R]$	$\lambda\,[R]$	$\eta\,[R]$	$T_0\,[T]$	Re_λ	$k_{\max}\eta$	Tethered	Free
A	0.16	0.77	0.25	0.013	3.67	90	1.72	4	3
	0.33	0.77	0.18	0.008	0.19	129	1.07	5	16
	0.60	0.76	0.13	0.005	0.98	177	0.99	9	9
	0.99	0.76	0.11	0.004	0.62	227	0.94	27	6
B	0.33	1.54	0.26	0.01	3.62	186	1.32	10[a]	–
	0.33	0.77	0.18	0.008	1.91	129	1.07	5	16
	0.33	0.32	0.11	0.006	0.77	82	1.70	5	15

[a]We computed two runs with four insects and an additional two runs with only one and two additional runs with only one insect.

C. Bumblebee model

In our numerical simulations, we use a model bumblebee in forward flight at $u_\infty = 2.5\,\mathrm{m/s}$ as archetype for medium-sized insects. The Reynolds number is $\mathrm{Re} = \overline{U}_{\mathrm{tip}} c_m/\nu_{\mathrm{air}} = 2060$, where $\overline{U}_{\mathrm{tip}} = 2\Phi R f = 8.05\,\mathrm{m/s}$ is the mean wing-tip velocity, $c_m = 4.012\,\mathrm{mm}$ is the mean chord length, $\nu_{\mathrm{air}} = 1.568\times10^{-5}\,\mathrm{m^2/s}$ is the kinematic viscosity of air, $R = 1.32\times10^{-2}\,\mathrm{m}$ is the wing length, $f = 152\,\mathrm{Hz}$ ($T = 1/f = 6.6\,\mathrm{ms}$) is the wing-beat frequency (T is duration), and $\Phi = 115^\circ$ is the wing-beat amplitude. The model is described in greater detail elsewhere [16, Suppl. Mat.]. The mass of the insect is $m = 175\,\mathrm{mg}$, the gravitational acceleration $g = 9.81\,\mathrm{m/s^2}$, and the moments of inertia of the body are $J^{(b)}_{\mathrm{roll}} = 1.14\times10^{-9}\,\mathrm{kg\,m^2}$, $J^{(b)}_{\mathrm{yaw}} = 4.33\times10^{-9}\,\mathrm{kg\,m^2}$, and $J^{(b)}_{\mathrm{pitch}} = 4.18\times10^{-9}\,\mathrm{kg\,m^2}$. We use the superscript $^{(b)}$ when referring to the body reference frame.

We perform two types of simulations, one where the insect is anchored to the virtual wind tunnel (tethered flight) and one where its motion is computed from fluid forces and moments (free flight) as well as gravity. The governing equation for the free flight case is Newton's second law of motion

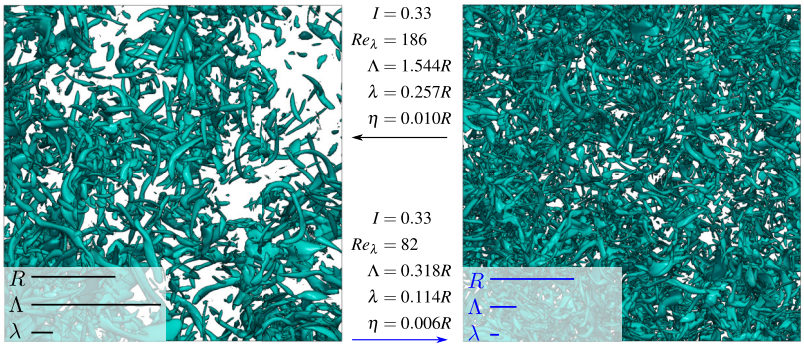

FIG. 4. Two HIT fields from the series B, both with identical turbulent kinetic energy (and hence turbulence intensity I). Visualized is the isosurface $|\underline{\omega}| = 4\sigma(\underline{\omega})$ of vorticity magnitude, where σ is the standard deviation. Insets show visual comparison of wing length R, integral scale Λ, and Taylor microscale λ.

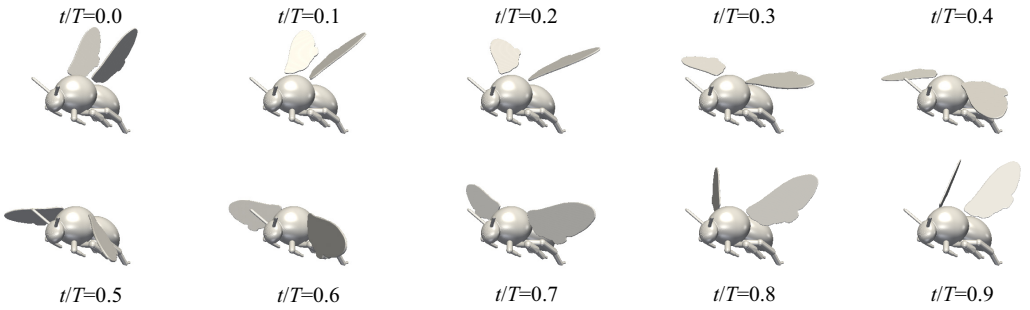

FIG. 5. Visualization of the bumblebees prescribed flapping motion every $0.1T$ time steps.

for linear and angular motion. For the latter, we use a quaternion ansatz to avoid the Gimbal lock problem. Gimbal lock occurs when two rotation axis become parallel and the system loses one degree of freedom. The detailed set of 13 first-order ODEs can be found in Ref. [42]. In both free and tethered flight, we prescribe an identical wing motion relative to the body, as illustrated in Fig. 5. The wing motion is identical for all wing beats. The wings and body are assumed to be rigid.

Our bumblebee model responds in the free flight case, unlike real animals, entirely passively to perturbations. Therefore, we limit the simulation time to the order of magnitude of the reaction time delay τ_{react} in those animals. After this delay, the insect may employ active steering mechanisms and modify the wing beat or body posture. Previous studies on freely flying honeybees reported response delays of approximately 20 ms or 4.5 stroke cycles, suggesting the use of ocellar pathways for body stability reflexes in this species [48]. By contrast, recent work [26] suggests reaction times of about 5 ms in fruit flies. The precise delay in bumblebees is unknown but expected to be of the same order of magnitude as in honeybees. Therefore, we simulate eight stroke cycles (52.6 ms) in a simulation, thus allowing quantification of the response for any $\tau_{\text{react}} \leqslant 8T$. Notably, we do not know exactly under which conditions insects react at all to perturbations, or simply accept the externally imposed change in flight direction and orientation. An example for this is shown in Ref. [14], where bumblebees are found to ignore aerial perturbations when approaching a cylinder.

D. Governing equations and numerical method

The present work relies on numerical simulations. We directly solve the incompressible Navier-Stokes equations without any *a priori* turbulence models. All scales of fluid motion are fully resolved in time and space. In this section, we describe briefly the numerical method we use, for reasons of self-consistency. For further details, the reader is referred to Ref. [42].

We employ a Fourier pseudospectral method for spatial discretization and a second-order Adams-Bashforth scheme for time advancement. The spectral discretization is fast and accurate [49] and is particularly useful in our case as the Laplace operator becomes diagonal in Fourier space. Hence, the solution of a Poisson problem is trivial in Fourier space. To include the no-slip boundary conditions on the time-varying geometry we use the volume penalization method [50]. This allows us to maintain the advantages of the Fourier discretization. Hence, we solve the penalized Navier-Stokes equation

$$\partial_t \underline{u} + \underline{\omega} \times \underline{u} = -\boldsymbol{\nabla} \Pi + \nu \nabla^2 \underline{u} - \underbrace{\frac{\chi}{C_\eta}(\underline{u} - \underline{u}_s)}_{\text{penalization}} - \underbrace{\frac{1}{C_{\text{sp}}} \boldsymbol{\nabla} \times \frac{(\chi_{\text{sp}} \underline{\omega})}{\nabla^2}}_{\text{sponge}}, \tag{1}$$

$$\boldsymbol{\nabla} \cdot \underline{u} = 0, \tag{2}$$

$$\underline{u}(\underline{x}, t = 0) = \underline{u}_0(\underline{x}), \quad \underline{x} \in \Omega, t > 0, \tag{3}$$

where $\underline{u}$ is the fluid velocity and $\underline{\omega} = \nabla \times \underline{u}$ is the vorticity. We normalize the density ρ_f to unity. The nonlinear term in Eq. (1) is written in the rotational form. Hence, we are left with the gradient of the total pressure $\Pi = p + \frac{1}{2}\underline{u} \cdot \underline{u}$ instead of the static pressure p [49]. This formulation is chosen because of its favorable properties when discretized with spectral methods, namely conservation of momentum and energy [49, p. 210]. At the exterior of the computational domain, we assume periodic boundary conditions. The domain is sufficiently large to minimize the effect of periodicity.

The mask function χ is defined as

$$\chi(\underline{x}, t) = \begin{cases} 0 & \text{if } \underline{x} \in \Omega_f \\ 1 & \text{if } \underline{x} \in \Omega_s \end{cases}, \tag{4}$$

where Ω_f is the fluid and Ω_s is the solid domain. Note that in the fluid domain Ω_f, the original equations hold as the penalization term $\frac{\chi}{C_\eta}(\underline{u} - \underline{u}_s)$ vanishes. The convergence proof in Refs. [50,51] shows that the solution of the penalized Navier-Stokes equations (1)–(3) tends for $C_\eta \to 0$ indeed toward the exact solution of Navier-Stokes imposing no-slip boundary conditions. Here, we use $C_\eta = 2.5 \times 10^{-4}$. We also add a second penalization term for the vorticity $\underline{\omega}$, which we call sponge term. The sponge gradually damps the vorticity in regions where $\chi_{\text{sp}} = 1$. The sponge constant is set to $C_{\text{sp}} = 10^{-1}$.

In the case of free flight, we compute the position and orientation of the insect from the aerodynamic forces and moments using a quaternion-based formulation. We integrate the resulting ODE system time using the same Adams-Bashforth scheme as for the fluid. More details about the numerical method and its implementation in the open-source code FLUSI [52] can be found in Ref. [42], along with detailed validation cases. In addition, Appendix shows the convergence of the forces for decreasing wing thickness of a flapping wing.

III. RESULTS AND DISCUSSION

In the following subsection, we present and discuss the results of two types of simulations, tethered and free flight. We use both cases to investigate the influence of turbulence on the insect when varying either the intensity or the length scales of the turbulent inflow perturbations. We start with the tethered cases, which serve as references for the free flight cases. In numerical simulations, the tethered case is the idealized limit of perfect control. In experimental work, where the animals are fixed using a material tether, usually a thin wire glued to the back, the insects lack the sensor feedback present in free flight. The wing kinematics might then be very different from what an insect uses in free flight [53]. However, note that our tethered simulations are based on wing kinematics measured in free flight [54,55]. They are thus equivalent to a tethered insect that flaps as if it were in free flight.

A. Tethered flight

1. Influence of turbulence intensity at fixed length scales

We first study the influence of I at constant integral scale Λ. The insect is tethered and we used the series A of turbulence fields, as presented in Ref. [16]. Their properties are summarized in Table I. We fix the integral scale and vary the turbulence intensity I, which also results in an increasing Reynolds number Re_λ and reduced eddy turnover time. Figure 6 illustrates the obtained results for forces [Figs. 6(a)–6(c)], moments [Figs. 6(d)–6(f)], and aerodynamic power [Fig. 6(g)]. We choose the box plot representation, first introduced in Ref. [56], to visualize the data. Each of the N_R realizations yields N_w independent cycle-averaged forces and moments (Table I). The median value of the data are remarkably close to the value in the laminar case (dashed line) for all quantities, even in the strongest inflow turbulence. This indicates that turbulence does not systematically alter the vortex dynamics generated by the flapping wings of the insect. This vortex system features the leading edge vortex that results from the typically high angle of attack (here roughly 50°) [57–59]. The leading-edge vortex remains attached to the wing in unperturbed conditions, and in the simulations with turbulent inflow it is not systematically detaching neither. Owing to the decreased

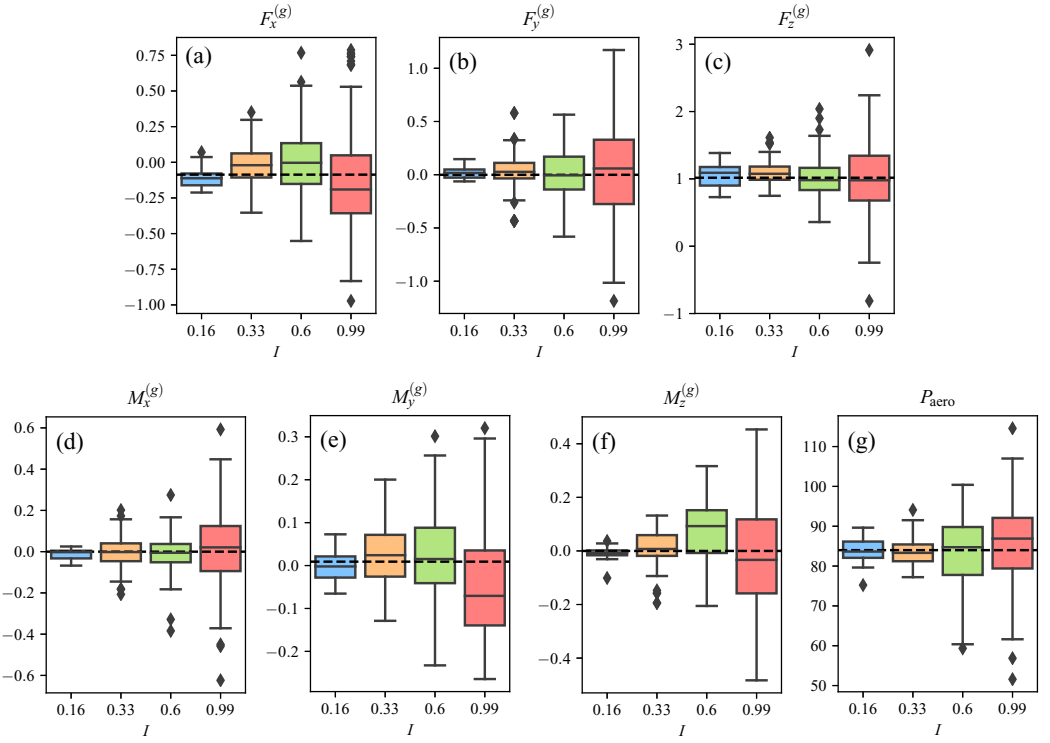

FIG. 6. Tethered flight in turbulence. The integral scale is $\Lambda = 0.77R$ and I varies between 0 and 0.99. Cycle averaged values are represented by box plots. Each of the N_R simulations yields four data points, one for each cycle. In the colored boxes, the line is the median (or two-quantile) of the data, and the limits of the box are the upper and lower quartiles (or four-quantile). The additional vertical line are min/max values excluding outliers, which are shown as individual points with a $\diamond$ marker. Aerodynamic quantities are forces [(a)–(c), normalized by mg], moments [(d)–(f), normalized by mgR], and aerodynamic power [(g), in W/kg body mass]. The dashed line corresponds to the laminar case ($I = 0$) where the insect is aligned with the mean flow.

pressure in its core, this vortex provides a boost for the aerodynamic forces, especially the lift force. Thus, its detachment or destruction would result in a significant change in forces, moments, and power. Compared to an airfoil, where upstream turbulence can trigger transitions in the boundary layer or impact flow separation, this behavior is thus different. However, fluctuations occur, as represented in Fig. 6 by the colored boxes and the min-max values. With increasing turbulence intensity, those fluctuations become larger. We conclude that flapping flight in turbulence faces insects more with a problem for control rather than deteriorated force production [16].

2. Influence of turbulent length scales at constant intensity

With the results of Ref. [16], we now further explore the influence of turbulent length scales on tethered flight and use the series B from Table I, where we fixed $I = 0.33$. This particular intermediate value of I does not require a large number of flow realizations for any tested value of Λ, which allows keeping the computational cost within acceptable limits. Furthermore, field experiments [17] show a large flight activity of bumblebees for this value of I.

Figure 7 illustrates the cycle-averaged forces, moments, and power as a function of Λ. The median values are close to the values in laminar inflow (dashed line), which is consistent with the findings in Ref. [16] and Fig. 6. For any quantity, fluctuations are significantly reduced at

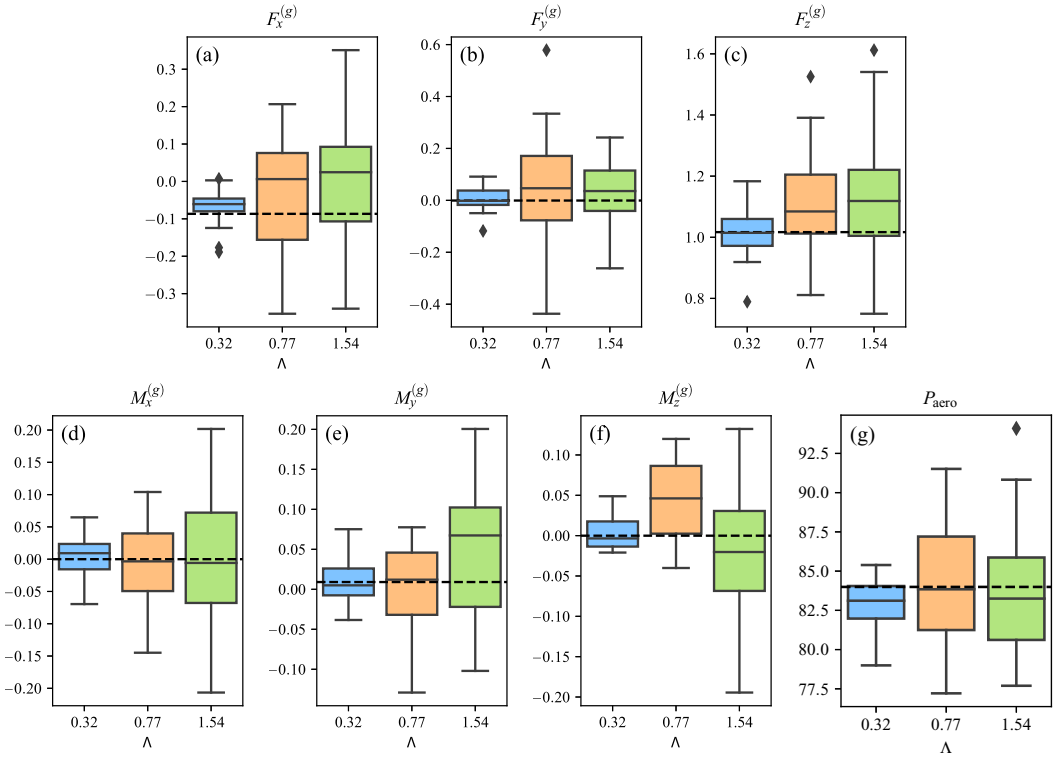

FIG. 7. Tethered flight in turbulence. The turbulence intensity is $I = 0.33$ and the integral scale Λ varies between $0.32R$ and $1.54R$. Cycle averaged values are represented by box plots. Each of the N_R simulations yields four data points, one for each cycle. In the colored boxes, the line is the median of the data, and the limits of the box are the upper and lower quartiles. The additional vertical line are min-max values excluding outliers, which are shown as individual points with a ◇ marker. Aerodynamic quantities are forces [(a)–(c), normalized by mg], moments [(d)–(f), normalized by mgR], and aerodynamic power [(g), in W/kg body mass]. The dashed line corresponds to the laminar case ($I = 0$) where the insect is aligned with the mean flow.

$\Lambda = 0.32R$ (blue), compared to the other two cases. The lateral [Fig. 7(b)] and lift [Fig. 7(c)] forces exhibit the largest fluctuations for $\Lambda = 0.77R$, while the fluctuations in thrust [Fig. 7(a)] are of the same magnitude in both cases. For the aerodynamic torques [Figs. 7(d)–7(f)], the largest fluctuations appear for $\Lambda = 1.54R$ with standard deviations $\sigma = 0.104, 0.095$, and 0.076 for the roll (M_x), pitch (M_y), and yaw (M_z) moments, respectively. The yaw moment is slightly less sensitive to perturbations but remains of the same order of magnitude. The aerodynamic power P_{aero} [Fig. 7(g)] displays the same behavior as the forces, with $\Lambda = 0.77R$ resulting in the largest fluctuations. However, in that case, $\sigma(P_{\text{aero}})/\overline{P}_{\text{aero}} = 0.05$, while for the vertical force $\sigma(F_z)/\overline{F}_z = 0.2$. The power thus fluctuates little.

These results suggest a reduced sensitivity to turbulence at smaller scales, expressed in a reduction of more than a factor of 2 in the magnitude of fluctuations at the same turbulence intensity. This is in agreement with the conjecture stated in Ref. [13] that perturbations which are small compared to the animal average out over the body and thus induce less perturbations. To further explore the effect of Λ, we illustrate in Figs. 8(a) and 8(b) the flow for the coarsest and finest turbulent case. Vortical structures are visualized by the Q criterion [60]. For both inflow conditions, we plot the same relative isosurface using the standard deviation σ, $Q = 0.7\sigma(Q)$, to identify vortices. In the coarser turbulence, less vortex tubes can be identified in the region between the inlet and the insect than in the smaller scale case, and the tubes are of similar diameter. This

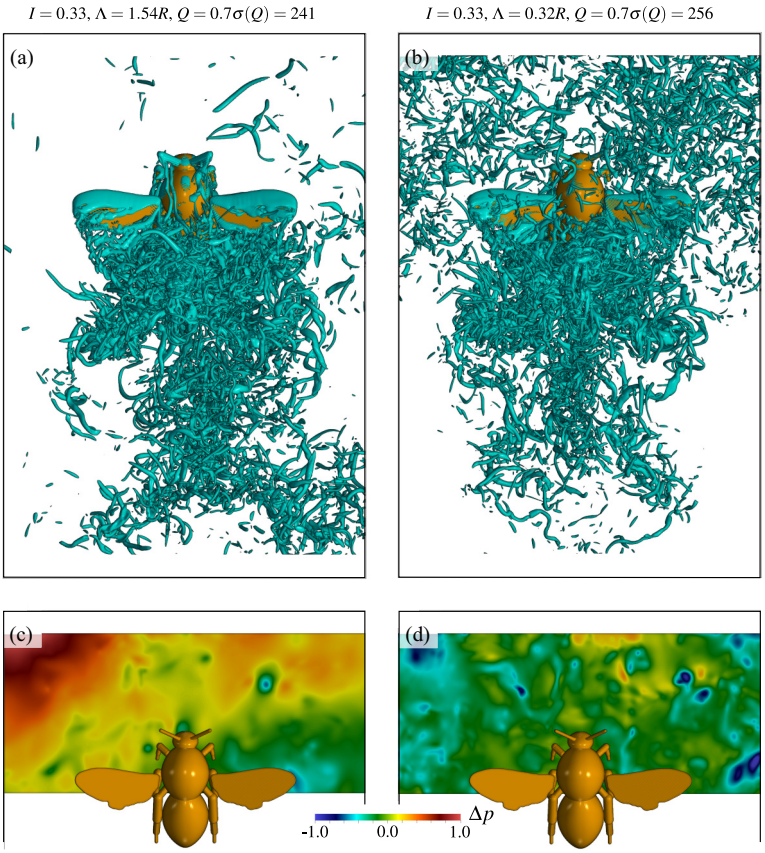

FIG. 8. Tethered flight in turbulence. Left column, $I = .33$ and $\Lambda = 1.54R$; right column, $I = .33$ and $\Lambda = 0.32R$. [(a), (b)] An isosurface of the Q criterion is shown to visualize vortical structures. In the case of $\Lambda = 1.54R$ (a), fewer vortices are identified upstream of the insect. [(c), (d)] Corresponding pressure field, where the pressure from the laminar inflow has been subtracted, $\Delta p = p_{\text{turb}} - p_{\text{lam}}$. Compared to the $\Lambda = 0.32R$ case (d), variations in pressure are of the same order of magnitude but on a larger spatial scale in the $\Lambda = 1.54R$ case (c).

may lead to the visual intuition that the smaller scale turbulence has a larger impact on the insect. However, the pressure field, illustrated in Figs. 8(c) and 8(d) as the difference in pressure between the turbulent and laminar realization, $\Delta p = p_{\text{turb}} - p_{\text{lam}}$, confirms that pressure fluctuations are of similar magnitude in both cases, while the spatial scale differs significantly. The coarser scale turbulence is associated with much larger scales of the pressure variations, which therefore have less chance of canceling out over the region of the insect.

B. Free flight

We now consider our model in free flight with all six degrees of freedom coupled to the flow solver, neglecting active control. This configuration is more realistic for real insects, since they cannot react instantaneously to changes in the flow condition. Reaction rather takes place after a time delay τ_{react}, during which sensor information is converted to changes in wing beat for active countermeasures (see Sec. II C). Therefore, the insect behaves passively during this interval, similar to what our model does. The orientation and linear and angular velocities after τ_{react} can thus yield insight into the effort required for corrective maneuvers.

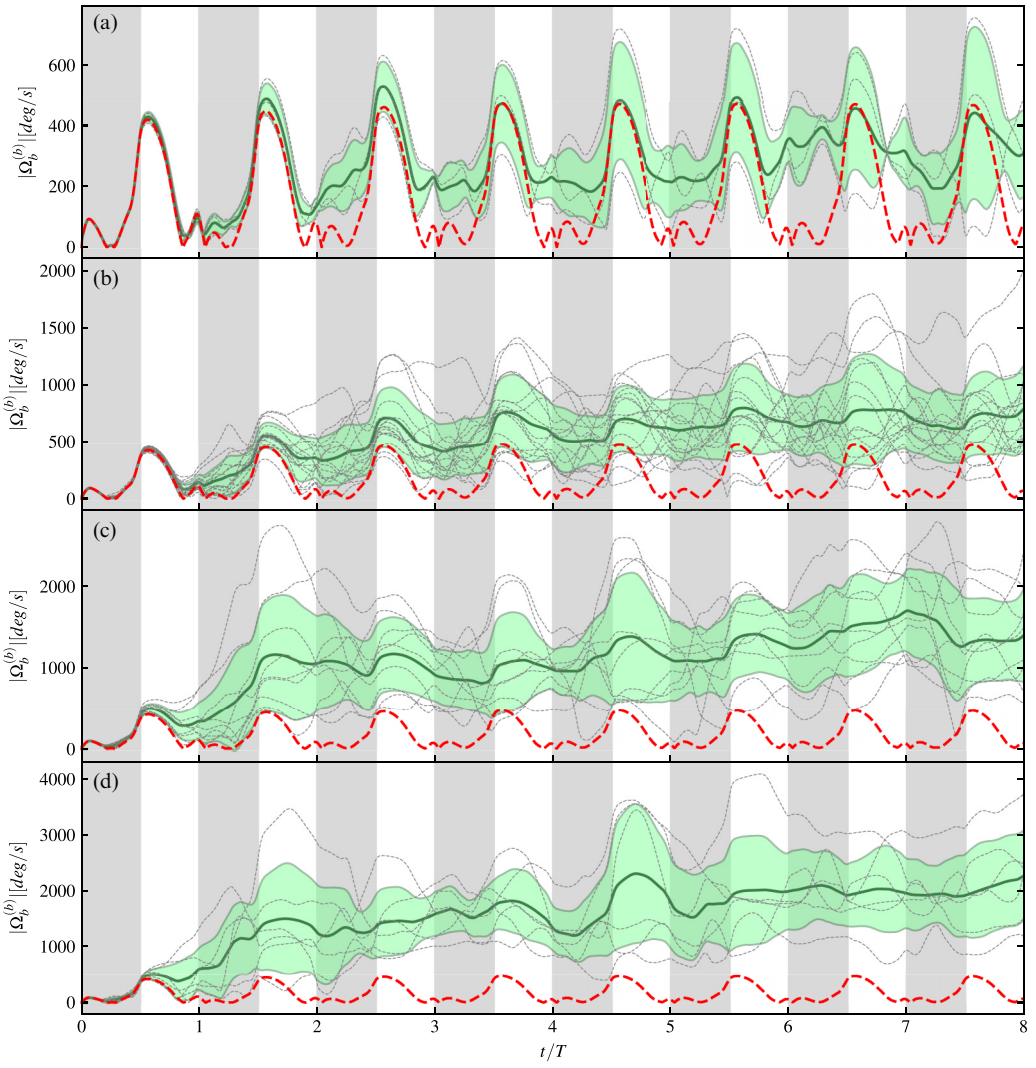

FIG. 9. Free flight in turbulent inflow, $I = 0.16$ (a), 0.33 (b), 0.60 (c), and 0.99 (d), for fixed $\Lambda = 0.77$. Time evolution for the magnitude of body angular velocity. Individual realizations are shown as thin, gray, dashed lines. Ensemble averaged time evolution is represented by the thick green line and the light green shaded background illustrates the standard deviation. The red dashed line corresponds to the laminar case.

1. Influence of turbulence intensity at constant length scales

After revisiting the problem of a tethered bumblebee in turbulence and studying the same model in free flight and laminar inflow, we now turn to free flight in turbulence. We first keep $\Lambda = 0.77R$ fixed for these simulations and alter the energy content of the imposed velocity fluctuations (series A in Table I). In free flight, force and moment fluctuations are transduced to linear and angular velocities, which in turn alter the forces and moments. It can be seen as the limiting case of no flight control, while tethered flight can somehow be seen as a limit of perfect control using external force, in the sense that attitude is perfectly stabilized while neglecting the necessary changes in wing beat.

Figures 9(a)–9(d) show the magnitude of the body's angular velocity, $\underline{\Omega}_b^{(b)}$, as a function of time for the four different turbulence intensities $I = 0.16$, 0.33, 0.60, and 0.99. At the lowest turbulence

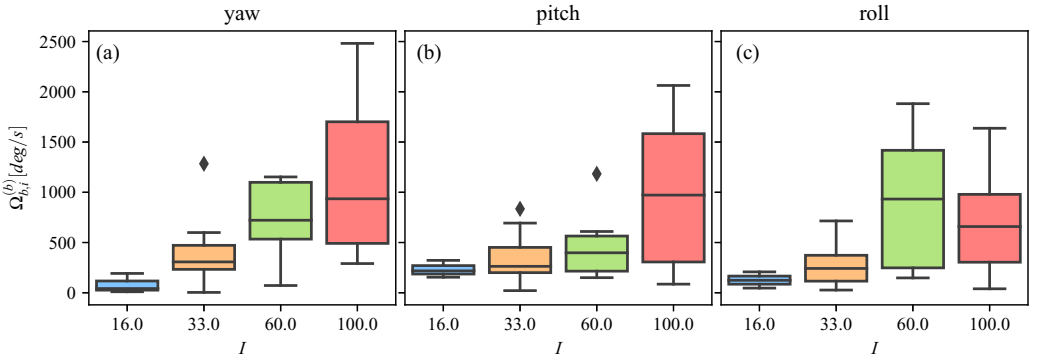

FIG. 10. Free flight in turbulent inflow. Shown are the yaw (a), pitch (b), and roll (c) components of the body angular velocity, averaged over the last computed cycle, as a function of the turbulence intensity. Data are represented by a box plot. In the colored boxes, the line is the median of the data, and the limits of the box are the upper and lower quartiles. The additional vertical line correspond to min-max values excluding outliers (◇).

intensity [Fig. 9(a)], fluctuations remain small and the overall time evolution resembles the laminar case, in which only the pitch component of $\underline{\Omega}_b^{(b)}$ is nonzero owing to lateral symmetry, although the difference grows in time. The first stroke is virtually unaffected as perturbations have not yet been advected to the insect. From the next larger value of I in Fig. 9(b), the resemblance to the laminar case disappears. The terminal value of the ensemble averaged angular velocity increases from $829^\circ/\mathrm{s}$ at $I = 0.33$ [Fig. 9(b)] to $2300^\circ/\mathrm{s}$ at $I = 0.99$ [Fig. 9(d)]. In the laminar case, peak values of $470^\circ/\mathrm{s}$ are found. It can be seen that after an initial growth phase, which takes place roughly in the first two strokes, the average angular velocity remains roughly constant; thus, it is limited by aerodynamic damping.

Figure 10 shows the components of the angular velocity vector, averaged over the last cycle $7 \leqslant t/T \leqslant 8$, as a function of the turbulence intensity. The magnitude of the mean value as well as fluctuations increase with increasing I, but no relevant difference among the three directions can be observed. We thus do not observe a significantly increased roll angular velocity [Fig. 10(c)], despite the lower moment of inertia around this axis.

We find the largest magnitude of linear velocity $|\underline{u}_b^{(b)}|/u_\infty = 0.06 \pm 0.04$ for the highest turbulence intensity ($I = 0.99$, $\Lambda = 0.77R$). It can be concluded that, even for the largest turbulence intensity, the translational response of the bumblebee is small compared to the flight speed. Therefore, the changes in position $\underline{x}_{\mathrm{cntr}}$ are small within the time span of the computations, i.e., $8T$. The impact of turbulence on the angular degrees of freedom is thus much higher than on the linear ones.

2. Influence of turbulent length scales at constant intensity

As for the tethered case, we fix $I = 0.33$ and vary the integral scale Λ of the turbulent inflow perturbations. Figure 11 shows the angular velocity components for the case $I = 0.33$, $\Lambda = 0.77R$ [Figs. 11(a)–11(c)] and $\Lambda = 0.32R$ [Figs. 11(d)–11(f)]. Each realization is shown as a thin gray line, and the reference computation in laminar flow is shown as red dashed line. All realizations result in a different attitude of the insect, though the turbulence fields have identical statistical properties. The ensemble-averaged time evolution (solid green lines) is however remarkably close to what is seen in laminar inflow. Standard deviations among the realizations (green shaded area) increase with time, as turbulent inflow perturbations are imposed continuously.

Ensemble-averaged angular orientation, expressed in term of the body angles, does not change significantly for ψ_{roll} and ψ_{yaw}, while β_{pitch} has changed by 8.5°. Fluctuations are largest for yaw

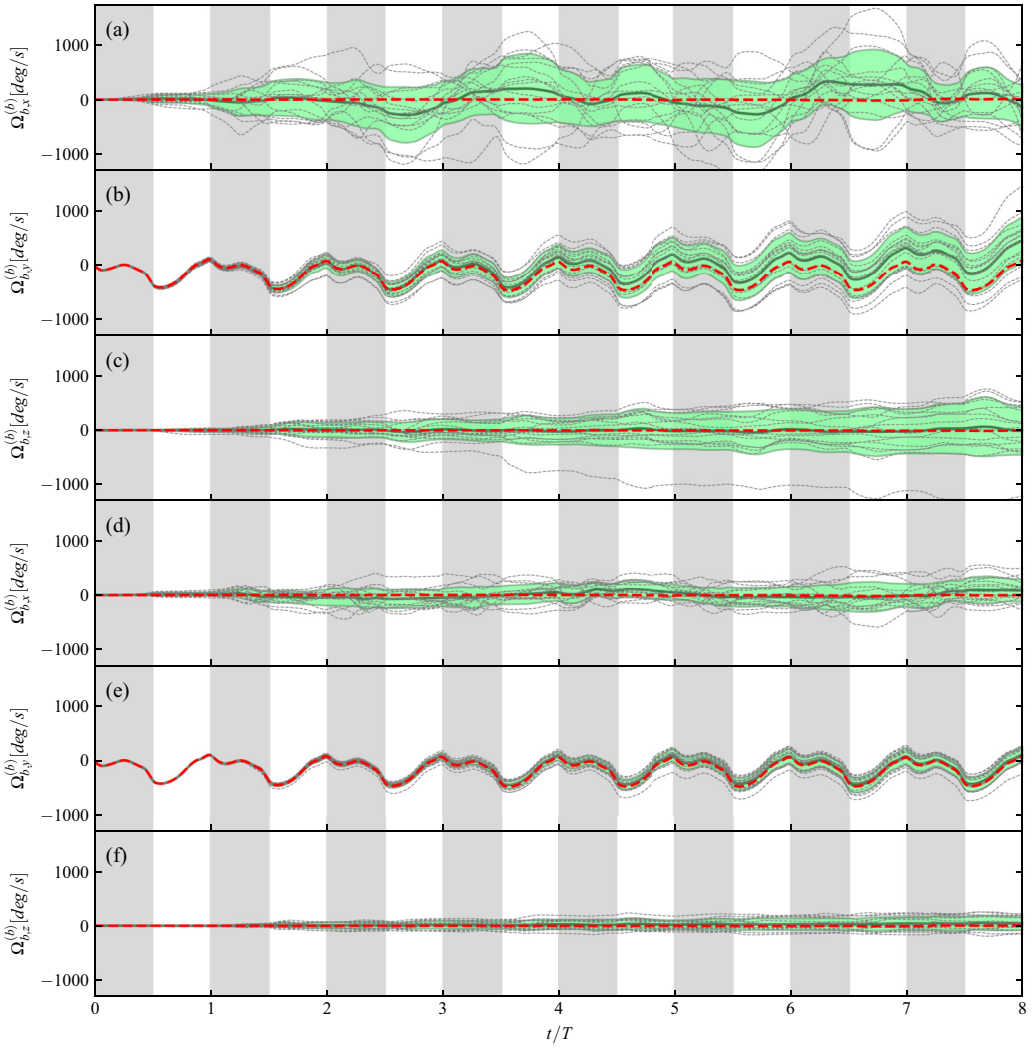

FIG. 11. Free flight in turbulent inflow, $I = 0.33$: [(a)–(c)] $\Lambda = 0.77R$ and [(d)–(f)] $\Lambda = 0.32R$. Time evolution of the three components of the angular velocity vector of the body, in the body system $\underline{\Omega}_b^{(b)}$. Angular velocities are given in $^\circ/s$ for easier comparison with results in the literature. Individual realizations are shown as thin gray lines. Ensemble-averaged time evolution is represented by the thick green line, and light green shaded background illustrates the standard deviation. The thick red dashed line corresponds to the laminar case.

(15.4°), followed by pitch (11.0°) and roll (10.3°). The values are, however, close to each other, such that the difference is not significant.

For all components, the standard deviation of the angular velocity $\underline{\Omega}_b^{(b)}$ first grows in time, until some saturation is reached. The initial growth rate is largest for the roll component [Fig. 11(a)], which presents large fluctuations at $t = 2T$ already. By this time, the pitch component [Fig. 11(b)] has almost vanishing fluctuations and those in yaw [Fig. 11(c)] are significantly smaller. The insect's motion is damped by the viscous fluid, and thus the magnitude of the angular velocity remains bounded.

Figures 11(d)–11(f) show the same quantities as Figs. 11(a)–11(c) for the case $\Lambda = 0.32R$. While the qualitative behavior is similar, the magnitudes of both changes in angular orientation and angular

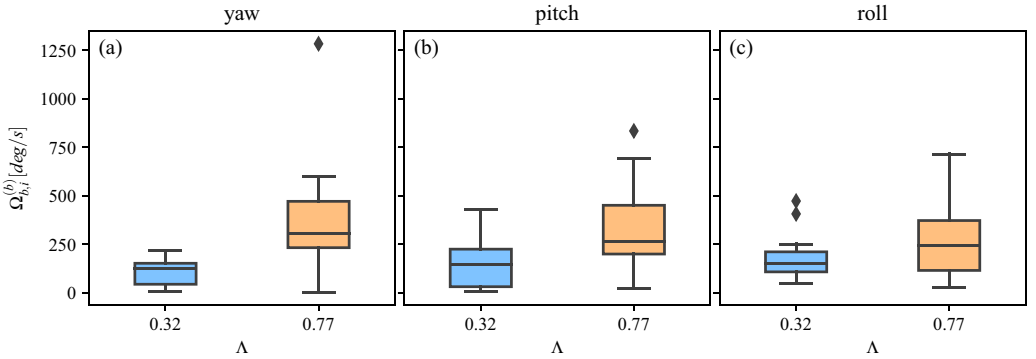

FIG. 12. Free flight in turbulent inflow. Yaw (a), pitch (b), and roll (c) components of the body angular velocity, averaged over the last computed cycle, as a function of Λ. Data are represented by a box plot. In the colored boxes, the line is the median of the data, and the limits of the box are the upper and lower quartiles. The additional vertical line is min-max values excluding outliers (◇).

velocities of the body ($\underline{\Omega}_b^{(b)}$) are significantly reduced. For example, $\gamma_{\text{yaw}} = 20^\circ$ in the $\Lambda = 0.77R$ case is reduced to 2.5°. The fluctuations in roll angular velocity grow quickest.

From the direct comparison of the two cases, we can confirm the conclusions from the tethered simulations also in the free flight case. The reduced integral scale significantly reduces the impact of the flow on the insect's attitude. Figure 12 shows the magnitude of the different components of the angular velocity and confirms that conclusion. Furthermore, as the 95% confidence intervals of the different directions overlap for both values of Λ, again no direction with statistically significantly increased magnitude can be observed. It appears thus from Fig. 11 that while the roll angular velocity grows quickest, its terminal value is not significantly larger than the other two components, yaw and pitch.

A key advantage of numerical work is that we can exclude any voluntary motion that might be used, e.g., for distance estimation [14]. However, at this point, we cannot give a quantitative estimate for the limit of stable flight in turbulent conditions. The first uncertainty concerns the degree of desired control. Experimental work [14] suggests that bumblebees passively ride out small-scale perturbations and actively impose a long-wavelength casting motion. It thus seems that real animals are somewhat behaving between the two limiting cases of tethered and free flight. This can also result from energetic considerations as allowing for a certain amount of deviations may reduce overall energetic cost.

The role of the reaction time delay appears to be the second crucial factor for evaluating the stability. Our free flight data show that fluctuations in angular velocity grow quickest for the roll axis, which is a consequence of the reduced moment of inertia. Figures 11(a) and 11(c) show that the roll component has reached its saturation at about $t = 2T$. Beyond this time, damping inhibits further growth, possibly via the flapping countertorque (FCT) mechanism [18,61]. This does not imply any bound for changes in body angles, which continuously grow in time. However, without the damping, the angular velocities are expected to grow continuously, leading to much greater changes in orientation.

Experimental work [48] showed that honeybees (*Apis mellifera*) use angular velocities for roll, pitch, and yaw of 3090, 697, 1874 °/s, respectively, during the active recovery phase after being perturbed with a strong wind gust. The magnitude of this angular velocity is 3680 °/s, which is higher than the largest value we find in our simulations (Fig. 9) and also higher than the 2060 °/s reported in Ref. [48] during the passive phase directly after the perturbation. The associated reaction time is stated as $3.5T < \tau_{\text{react}} < 6T$. Besides differences in species (we are not aware of data available for bumblebees in the literature), the study cannot directly be used to define a threshold

for the angular velocity beyond which the animals cannot recover. In addition, flying in turbulence imposes continuous perturbations, while the authors of Ref. [48] studied the effect of a singular gust.

IV. CONCLUSIONS AND PERSPECTIVES

We numerically studied the impact of turbulence on a model insect, using high-resolution numerical simulations on massively parallel machines. Both tethered and free flight without control have been considered, using a bumblebee model with rigid wings and prescribed wing-beat kinematics. The inflow condition ranged from laminar to turbulent, and in the latter we varied the turbulence intensity as well as the spectral distribution of the turbulent kinetic energy. For the turbulent inflows, we performed ensemble averaging to obtain statistical estimates of forces, moments, and power in the tethered case and body orientation and velocities in the free flight case.

In tethered flight, we have statistically estimated that the turbulent inflow does not induce the detachment of the leading-edge vortex. This is true even in the strongest turbulence case and has already been shown in our previous work [16]. In addition to the turbulence intensity, here we found the spectral distribution of turbulent kinetic energy to be a significant parameter to be taken into account. If the integral scale of the inflow is smaller than the wing length, we found that statistically perturbations are reduced for forces, moments, and power, compared to turbulent inflow with larger integral scale. We have demonstrated that the pressure field of the turbulent perturbations is associated likewise with large-scale variations if the integral scale is large. The positive- and negative-pressure perturbations have thus less chance of canceling out over the body, which induces larger fluctuations.

Using free flight simulations, we first checked that our model remains stable for laminar inflow condition. In turbulent inflow, we confirmed the finding from the tethered flight. We found that changes in body orientation and angular velocity are highly sensitive to variations in the turbulence spectrum. For constant turbulence intensity, a smaller integral scale results in much smaller angular velocities and changes in orientation. By modifying the turbulence intensity at fixed integral scale, we showed how the angular velocities increase when the perturbations become stronger. In all free flight simulations, we found the translation of the insect to be small compared to its rotational motion.

Collectively, our findings suggest that the scales of turbulent motion have a significant effect on the aerodynamics of flapping flight and should hence be considered in future contributions on this topic.

In perspective, we plan to overcome the limitations of the current study and specifically include the effects of both wing flexibility and flight control. Moreover, since our results have been obtained using a single species, namely a bumblebee, the generalization to other insects is another important direction for future work. Finally, we aim to replace the homogeneous isotropic turbulence, which is a valuable starting point, by generic turbulent flows even more relevant to insects, e.g., flower wakes.

ACKNOWLEDGMENTS

Financial support from the Agence nationale de la recherche (ANR Grant No. 15-CE40-0019) and Deutsche Forschungsgemeinschaft (T.E., J.S.: DFG Grant No. SE 824/26-1; F.L.: Grant No. LE 905/17-1), project AIFIT, is gratefully acknowledged. D.K. gratefully acknowledges financial support from the JSPS KAKENHI Grant No. JP18K13693. The authors were granted access to the HPC resources of IDRIS under the Allocation No. 2018-91664 attributed by GENCI (Grand Équipement National de Calcul Intensif). For this work, we were also granted access to the HPC resources of Aix-Marseille Université financed by the project Equip@Meso (No. ANR-10-EQPX- 29-01). T.E., K.S., M.F., F.L., and J.S. thankfully acknowledge financial support granted by the ministères des Affaires étrangères et du développement international (MAEDI) et de l' Education national

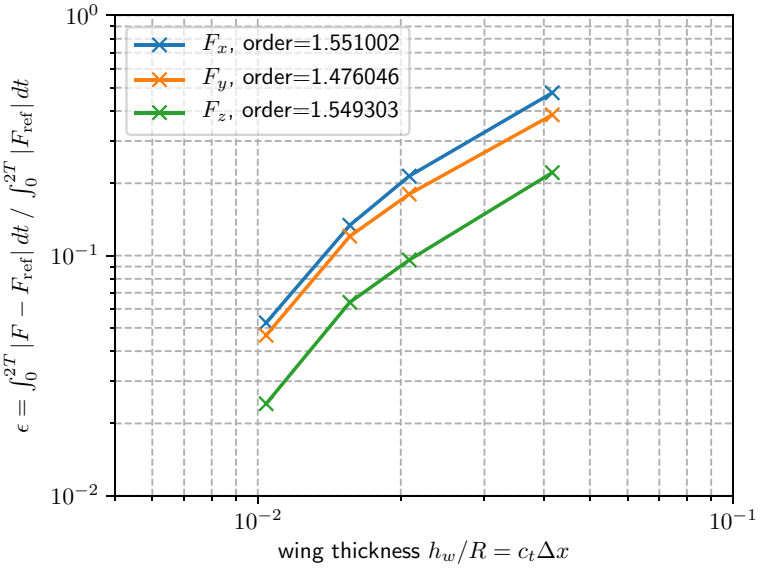

FIG. 13. Convergence of forces in the wing thickness.

et l'enseignement supérieur, de la recherche et de l'innovation (MENESRI), and the Deutscher Akademischer Austauschdienst (DAAD) within the French-German Procope project FIFIT.

APPENDIX: CONVERGENCE TO AN INFINITESIMALLY THIN FLAPPING WING

In this Appendix, we study the convergence of our numerical scheme in the limit of infinitesimally thin wings. We choose the same wing geometry as in the rest of the article, with the same kinematics, but simulate only one wing without the insect's body. The domain size is reduced to $2\times2\times2$ in order to be able to reach high resolutions. The thickness of the wing is $h_w/R = c_t\Delta x$ where we set the constant $C_t = 4$. As no reference solution is available, we instead use the solution on the finest grid. As described in Ref. [42], the penalization parameter $C_\eta = (K_\eta \Delta x)^2/\nu$ is reduced with increasing resolution, in order to achieve optimal results. The constant is $K_\eta = 7.4 \cdot 10^{-2}$. We perform five simulations with resolution 192^3, 384^3, 512^3, 768^3, and 1024^3, with h_w/R ranging from 4.2% to 0.78%. The error is evaluated as

$$\varepsilon = \int_0^{2T} (F_i - F_{\mathrm{ref},i})dt \Big/ \int_0^{2T} F_{\mathrm{ref},i}\,dt.$$

Figure 13 shows the resulting convergence. For all components, we find qualitatively the same behavior and an order of about 1.5. We can hence conclude that the penalization method retains its accuracy also in the limit of thin flapping wings.

[1] J. W. Chapman, V. A. Drake, and D. R. Reynolds, Recent insights from radar studies of insect flight, Annu. Rev. Entomol. **56**, 337 (2011).

[2] H. Liu, D. Kolomenskiy, T. Nakata, and G. Li, Unsteady bio-fluid dynamics in flying and swimming, Acta Mech. Sinica **33**, 663 (2017).

[3] S. B. Pope, *Turbulent Flows* (Cambridge University Press, Cambridge, UK, 2000).

[4] J. W. Chapman and V. A. Drake, in *Insect Migration, in Encyclopedia of Animal Behavior* (Elsevier, Amserdam, 2010), Vol. 2, pp. 161–166.
[5] J. Finnigan, Turbulence in plant canopies, Annu. Rev. Fluid Mech. **32**, 519 (2000).
[6] M. R. Raupach, Canopy transport processes, in *Flow and Transport in the Natural Environment: Advances and Applications*, edited by W. L. Steffen and O. T. Denmead (Springer, Berlin, 1988), pp. 95–127.
[7] M. R. Raupach and A. S. Thom, Turbulence in and above plant canopies, Annu. Ref. Fluid Mech. **13**, 97 (1981).
[8] J. C. Wyngaard, Atmospheric turbulence, Annu. Rev. Fluid Mech. **24**, 205 (1992).
[9] J. C. Wyngaard, *Turbulence in the Atmosphere* (Cambridge University Press, Cambridge, UK, 2010).
[10] V. M. Ortega-Jimenez, N. Sapir, M. Wolf, E. A. Variano, and R. Dudley, Into turbulent air: Size-dependent effects of von Kármán vortex streets on hummingbird flight kinematics and energetics, Proc. Biol. Sci. **281**, 20140180 (2014).
[11] T. L. Hedrick and T. L. Daniel, Flight control in the hawkmoth *Manduca sexta*: The inverse problem of hovering, J. Exp. Biol. **209**, 3114 (2006).
[12] V. M. Ortega-Jimenez, J. S. M. Greeter, R. Mittal, and T. L. Hedrick, Hawkmoth flight stability in turbulent vortex streets, J. Exp. Biol. **216**, 4567 (2013).
[13] S. Ravi, J. D. Crall, A. Fisher, and S. A. Combes, Rolling with the flow: Bumblebees flying in unsteady wakes, J. Exp. Biol. **216**, 4299 (2013).
[14] S. Ravi, D. Kolomenskiy, T. Engels, K. Schneider, C. Wang, J. Sesterhenn, and H. Liu, Bumblebee minimize control challenges by combining active and passive modes in unsteady winds, Sci. Rep. **6**, 35043 (2016).
[15] S. A. Combes and R. Dudley, Turbulence-driven instabilities limit insect flight performance, Proc. Natl. Acad. Sci. USA **106**, 9105 (2009).
[16] T. Engels, D. Kolomenskiy, K. Schneider, F.-O. Lehmann, and J. Sesterhenn, Bumblebee Flight in Heavy Turbulence, Phys. Rev. Lett. **116**, 028103 (2016).
[17] J. D. Crall, J. J. Chang, R. L. Oppenheimer, and S. A. Combes, Foraging in an unsteady world: Bumblebee flight performance in field-realistic turbulence, Interface Focus **7**, 20160086 (2017).
[18] T. L. Hedrick, B. Cheng, and X. Deng, Wingbeat time and the scaling of passive rotational damping in flapping flight, Science **324**, 252 (2009).
[19] S. A. Combes and T. L. Daniel, Flexural stiffness in insect wings I. Scaling and the influence of wing venation, J. Exp. Biol. **206**, 2979 (2003).
[20] A. R. Ennos, Inertial and aerodynamic torques on the wings of diptera in flight, J. Exp. Biol. **142**, 87 (1989).
[21] F. O. Lehmann, S. Gorb, N. Nasir, and P. Schützner, Elastic deformation and energy loss of flapping fly wings, J. Exp. Biol. **214**, 2949 (2011).
[22] T. Nakata and H. Liu, Aerodynamic performance of a hovering hawkmoth with flexible wings: A computational approach, Proc. Royal Soc. B: Biol. Sci. **279**, 722 (2012).
[23] T. Nakata and H. Liu, A fluid-structure interaction model of insect flight with flexible wings, J. Comput. Phys. **231**, 1822 (2012).
[24] G. Rüppell, Kinematic analysis of symmetrical flight manoeuvres of odonata, J. Exp. Biol. **144**, 13 (1989).
[25] R. Dudley, *The Biomechanics of Insect Flight: Form, Function, Evolution* (Princeton University Press, Princeton, NJ, 2002).
[26] T. Beatus and I. Cohen, Wing-pitch modulation in maneuvering fruit flies is explained by an interplay between aerodynamics and a torsional spring, Phys. Rev. E **92**, 022712 (2015).
[27] M. H. Dickinson and F. T. Muijres, The aerodynamics and control of free flight manoeuvres in drosophila, Philos. Trans. R. Soc. London, Ser. B **371**, 20150388 (2016).
[28] S. N. Fry, R. Sayaman, and M. H. Dickinson, The aerodynamics of free-flight maneuvers in Drosophila, Science **300**, 495 (2003).
[29] R. Berthé and F.-O. Lehmann, Body appendages fine-tune posture and moments in freely manoeuvring fruit flies, J. Exp. Biol. **218**, 3295 (2015).
[30] R. Noda, T. Nakata, and H. Liu, Body flexion effect on the flight dynamics of a hovering hawkmoth, J. Biomech. Sc. Engin. **9**, 14-00409 (2014).

[31] N. Yokoyama, K. Senda, M. Iima, and N. Hirai, Aerodynamic forces and vortical structures in flapping butterfly's forward flight, Phys. Fluids **25**, 021902 (2013).
[32] B. Cheng, S. N. Fry, Q. Huang, and X. Deng, Aerodynamic damping during rapid flight maneuvers in the fruit fly drosophila, J. Exp. Biol. **213**, 602 (2010).
[33] I. Faruque and J. S. Humbert, Dipteran insect flight dynamics, Part 2: Lateral-directional motion about hover, J. Theor. Biol. **265**, 306 (2010).
[34] B. Cheng and X. Deng, Translational and rotational damping of flapping flight and its dynamics and stability at hovering, IEEE Trans. Robot. **27**, 849 (2011).
[35] H. Liu, Integrated modeling of insect flight: From morphology, kinematics to aerodynamics, J. Comput. Phys. **228**, 439 (2009).
[36] H. Liu and K. Kawachi, A numerical study of insect flight, J. Comput. Phys. **146**, 124 (1998).
[37] M. Sun and J. Tang, Unsteady aerodynamic force generation by a model fruit fly wing in flapping motion, J. Exp. Biol. **205**, 55 (2002).
[38] J. Kim, D. Kim, and H. Choi, An immersed-boundary finite-volume method for simulations of flow in complex geometries, J. Comput. Phys. **171**, 132 (2001).
[39] A. Medina, J. D. Eldredge, J. Kweon, and H. Choi, Illustration of wing deformation effects in three-dimensional flapping flight, AIAA J. **53**, 2607 (2015).
[40] K. Hirohashi and T. Inamuro, Hovering and targeting flight simulations of a dragonfly-like flapping wing-body model by the immersed boundary-lattice Boltzmann method, Fluid Dyn. Res. **49**, 045502 (2017).
[41] K. Suzuki and T. Inamuro, Effect of internal mass in the simulation of a moving body by the immersed boundary method, Comput. Fluids **49**, 173 (2011).
[42] T. Engels, D. Kolomenskiy, K. Schneider, and J. Sesterhenn, FLUSI: A novel parallel simulation tool for flapping insect flight using a Fourier method with volume penalization, SIAM J. Sci. Comput. **38**, S3 (2016).
[43] D. Pekurovsky, P3DFFT: A framework for parallel computations of Fourier transforms in three dimensions, SIAM J. Sci. Comput. **34**, C192 (2012).
[44] T. Engels, D. Kolomenskiy, K. Schneider, and J. Sesterhenn, Numerical simulation of fluid-structure interaction with the volume penalization method, J. Comput. Phys. **281**, 96 (2015).
[45] T. Ishihara and Y. Kaneda, High resolution DNS of incompressible homogeneous forced turbulence—time dependence of the statistics, in *Statistical Theories and Computational Approaches to Turbulence* (Springer, Berlin, 2003), pp. 177–188.
[46] J. Jiménez, A. A. Wray, P. G. Saffman, and R. S. Rogallo, The structure of intense vorticity in isotropic turbulence, J. Fluid Mech. **255**, 65 (1993).
[47] R. S. Rogallo, Numerical experiments in homogeneous turbulence, NASA Tech. Memo. 81315, 1981.
[48] J. T. Vance, I. Faruque, and J. S. Humbert, Kinematic strategies for mitigating gust perturbations in insects, Bioinspir. Biomim. **8**, 016004 (2013).
[49] R. Peyret, *Spectral Methods for Incompressible Viscous Flow* (Springer, Berlin, 2002).
[50] P. Angot, C. Bruneau, and P. Fabrie, A penalization method to take into account obstacles in incompressible viscous flows, Numer. Math. **81**, 497 (1999).
[51] G. Carbou and P. Fabrie, Boundary layer for a penalization method for viscous incompressible flow, Adv. Diff. Equ. **8**, 1453 (2003).
[52] Available free of charge and without registration, https://github.com/pseudospectators/FLUSI
[53] R. B. Srygley and A. L. R. Thomas, Unconventional lift-generating mechanisms in free-flying butterflies, Nature (London) **420**, 660 (2002).
[54] R. Dudley and C. P. Ellington, Mechanics of forward flight in bumblebees I: Kinematics and morphology, J. Exp. Biol. **148**, 19 (1990).
[55] R. Dudley and C. P. Ellington, Mechanics of forward flight in bumblebees II: Quasi-steady lift and power requirements, J. Exp. Biol. **148**, 53 (1990).
[56] J. Tukey, *Exploratory Data Analysis* (Addison-Wesley, New York, 1977).
[57] C. P. Ellington, C. van den Berg, A. P. Willmott, and A. L. R. Thomas, Leading-edge vortices in insect flight, Nature (London) **384**, 626 (1996).

[58] C. P. Ellington, The novel aerodynamics of insect flight: Applications to micro-air vehicles, J. Exp. Biol. **202**, 3439 (1999).

[59] D. Kolomenskiy, Y. Elimelech, and K. Schneider, Leading-edge vortex shedding from rotating wings, Fluid Dyn. Res. **46**, 031421 (2014).

[60] J. C. R. Hunt, A. A. Wray, and P. Moin, Eddies, stream, and convergence zones in turbulent flows, Center for Turbulence Research Report CTR–S88, 1988.

[61] T. L. Hedrick, Damping in flapping flight and its implications for manoeuvring, scaling, and evolution, J. Exp. Biol. **214**, 4073 (2011).